

A Method for Simulating Spray Pyrolysis Deposition in the Level Set Framework

Lado Filipovic, *Member, IAENG*, Siegfried Selberherr, Giorgio C. Mutinati, Elise Brunet, Stephan Steinhauer, Anton Köck, Jordi Teva, Jochen Kraft, Jörg Siegert, Franz Schrank, Christian Gspan, and Werner Grogger

Abstract—The ability to deposit a thin tin oxide film on CMOS chip dies has enabled the manufacture of modern smart gas sensor devices. Spray pyrolysis deposition is used to grow the required thin films, as it is an affordable deposition technique which can be integrated into a standard CMOS processing sequence. A model for spray pyrolysis deposition is developed and implemented within the Level Set framework using Monte Carlo techniques. Two models for the topography modification due to spray pyrolysis deposition are presented, with an electric nozzle and a pressure atomizing nozzle. The resulting film growth is described as a layer by layer deposition of the individual droplets which reach the wafer surface and deposit as flat round disks or as a CVD-like process, depending on whether the droplets form a vapor near the interface or they deposit a film only after surface collision. Some additional geometries are simulated in order to analyze how the spray pyrolysis technique coats trench structures, essential for increasing the surface area of the gas sensing layer.

Index Terms—Spray pyrolysis deposition, Topography simulation, Level Set, Monte Carlo, Tin oxide film, Smart gas sensors

I. INTRODUCTION

The spray pyrolysis deposition technique is gaining traction in the scientific community due to its cost effectiveness and possibility of integration into a standard CMOS process. The technique is used to grow crystal powders [1], which can then be further annealed for use in fuel cells, gas sensors and other applications. This work examines two main applications of spray pyrolysis, those for electrolyte deposition in fuel cells and the deposition of a thin oxide sensing material on modern smart gas sensor devices. In addition, two modeling techniques are examined, which should be applied depending on the spray pyrolysis setup; the type of

atomizing nozzle and its placement with respect to the wafer surface play a significant role in deciding which model is appropriate [2]. The models are implemented in a Level Set framework using a combination of Monte Carlo methods for particle distribution.

A. Yttria-Stabilized Zirconia Deposition for Fuel Cells

The development of the solid oxide fuel cell (SOFC) stems from the desire to produce electrical energy directly from the chemical energy generated, when a fuel is oxidized. This process significantly reduces the emission of pollutants and improves the overall efficiency of power generation [3]. A sample schematic of a SOFC during operation is shown in Fig 1. The type of electrolyte determines the type of fuel cell.

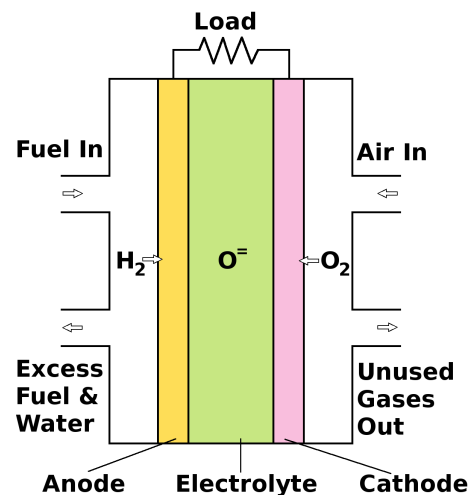


Fig 1. Schematic of a sample solid oxide fuel cell in operation.

The SOFC has an electrolyte which is comprised of a solid oxide or ceramic material such as yttria-stabilized zirconia (YSZ). Several fuel cell technologies are being developed simultaneously as the search for highly efficient and low polluting electricity production intensifies. A common type of fuel cell is one with a polymer electrolyte membrane (PEM) [4], which, unfortunately, has an expensive catalyst and is sensitive to fuel impurities [5]. Alkaline fuel cells (AFCs) [6] are very sensitive to CO_2 in the fuel as well as in air, while phosphoric acid fuel cells (PAFC) [7] provide a very low current and power [5]. These three types of fuel cells operate at low temperatures (typically below 200°C) and have a relatively low stack size (approximately 100kW). The two main types of high temperature and high power fuel cells are the molten carbonate fuel cell (MCFC) [8] and the

Manuscript submitted October 03, 2013;

This work has been partly performed in the COCOA-CATRENE European project and in the project ESiP (Funded by FFG No. 824954 and ENIAC). In this latter the Austrian partners are funded by the national funding institution for applied research and development in Austria, the Austrian Research Promotion Agency (FFG) under project no. 824954 and the ENIAC Joint Undertaking.

L. Filipovic and S. Selberherr are with the Institute for Microelectronics, Technische Universität Wien, Gußhausstraße 27–29/E360, A-1040 Wien, Austria (Phone: +43-1-58801-36036, Fax: +43-1-58801-36099 e-mail: filipovic|selberherr@iue.tuwien.ac.at).

G. C. Mutinati, E. Brunet, S. Steinhauer, and A. Köck are with Molecular Diagnostics, Health & Environment, AIT GmbH, Donau-City-Straße 1, A-1220 Wien, Austria (e-mail: Giorgio.Mutinati|Elise.Brunet.fl|Stephan.Steinhauer.fl|Anton.Koeck@ait.ac.at).

J. Teva, J. Kraft, J. Siegert, and F. Schrank are with ams AG, Tobelbaderstrasse 30, A-8141 Unterprenstätten, Austria (e-mail: Jordi.Teva|Jochen.Kraft|Joerg.Siegert|Franz.Schrank@ams.com).

C. Gspan and W. Grogger are with the Institute for Electron Microscopy and Fine Structure Research, Graz University of Technology and the Centre for Electron Microscopy Graz, Steyrergasse 17, A-8010 Graz, Austria (e-mail: christian.gspan@felmi-zfe.at|werner.grogger@felmi-zfe.at).

SOFC [9]. These types of fuel cells enjoy a higher efficiency and can be operated with a variety of different fuels and catalysts. The main advantage of SOFCs over MCFCs is a higher efficiency – 60% compared to 45-50%, respectively.

Deposition of thin oxides using the spray pyrolysis process is an inexpensive technique which can be utilized for the deposition of the electrolyte material for SOFCs. The process allows for a gas-tight YSZ ceramic film, with thicknesses between 0.1 and 10 μ m, to be grown on top of the anode, fulfilling the function of the electrolyte.

B. Tin-Oxide Based Gas Sensors

Different variants of metal oxide based gas sensors, which rely on changes of electrical conductance due to the interaction with the surrounding gas, have been developed. However, today's gas sensors are bulky devices, which are primarily dedicated to industrial applications. Since they are not integrated in CMOS technology, they cannot fulfill the requirements for smart gas sensor applications in consumer electronics. A powerful strategy to improve sensor performance is the implementation of very thin nanocrystalline films, which have a high surface to volume ratio and thus a strong interaction with the surrounding gases.

Two materials, which have been shown to exhibit all the properties required for good gas sensing performance are zinc oxide (ZnO) [10], [11], [12], [13] and tin dioxide (SnO₂) [14], [15], [16], while others such as indium tin oxide (ITO), CdO, ZnSnO₄, NiO, etc. have also been widely studied [12]. This work mainly concerns itself with tin dioxide gas sensors and the ability to develop a model which depicts the growth of thin tin dioxide layers to act as a gas sensing surface. The deposition of SnO₂ has been performed using various standard techniques, such as chemical vapor deposition [17], sputtering [18], pulsed-laser deposition [19], sol-gel process [20], and spray pyrolysis deposition [14].

Among the many gas sensing materials, tin oxide (SnO₂) has particularly proved to have a high potential for smart gas sensing devices and many SnO₂-based devices have already been realized [21], [22]. The growth of the ultrathin SnO₂ layers on CMOS structures requires a deposition step which can be integrated into the traditional CMOS process [15]. This alleviates the main concern with today's gas sensor devices, namely their high power consumption and complex manufacturing technique.

SnO₂ is a special material, as it has a low electrical resistance, a wide bandgap, and a high transparency in the visible spectrum [14]. The material has proven itself to be useful in many industries, where an electric contact is required without obstructing photons from traveling through the optical active area. Tin dioxide is also highly conductive due to high intrinsic defects.

A sensor which uses films with thicknesses of 50nm and 100nm has already been reported in [22]. The sensor itself operates on a micro-sized hot plate which heats the sensor locally to 250–400°C in order to detect humidity and carbon monoxide in the environment, down to a concentration of under 5ppm for CO. The sensing mechanism of SnO₂ is related to the ionosorption of gas species over the surface, leading to charge transfer between the gas and surface molecules and changes in the electrical conductance [22].

A smart gas sensor device has been manufactured using a 50nm SnO₂ thin film as the sensing material. The device has four electrodes, which are stationed above a heat source. The substrate is a CMOS chip with four contact electrodes which are coated with SnO₂, as depicted in Fig 2.

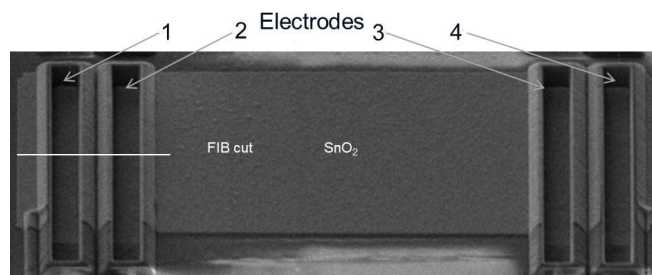


Fig 2. Top view of the electrode locations on the substrate.

The sensor has been tested in a H₂ environment at concentrations down to 10ppm and the results are depicted in Fig 3 and Fig 4. Additional gas sensing performance of SnO₂ thin films in a CO, CH₄, H₂, CO₂, SO₂, and H₂S environment are explored by Brunet et al. [16].

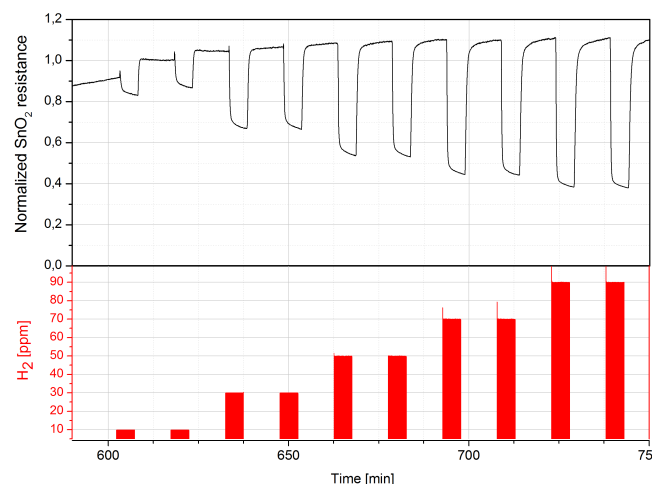


Fig 3. SnO₂ electrical resistance change as H₂ in varying concentration is pulsed into a humid synthetic air (RH=40%) environment. The sensing temperature is set to 350°C.

The gas measurements are performed in an automatic setup to test the functionality of the described SnO₂ structure, which is heated up at 350°C. The electrical resistance change is monitored, while pulses of H₂ at different concentrations (10–90ppm) are injected in the gas chamber. Humid synthetic air (RH=40%) is used as the background gas. In Fig 3 the normalized resistance of the SnO₂ structure is plotted for various H₂ gas concentrations. In Fig 4 the gas response, defined as the relative resistance difference in percentage, is shown. It is obvious that the SnO₂ resistance change corresponds to the change in H₂ concentrations. As the H₂ concentration is increased, the resistance of the SnO₂ thin film decreases. The gas sensor appears to be functional in the entire H₂ concentration range investigated.

C. Level Set Method

The presented simulations and models function fully within the process simulator presented in [23]. The Level

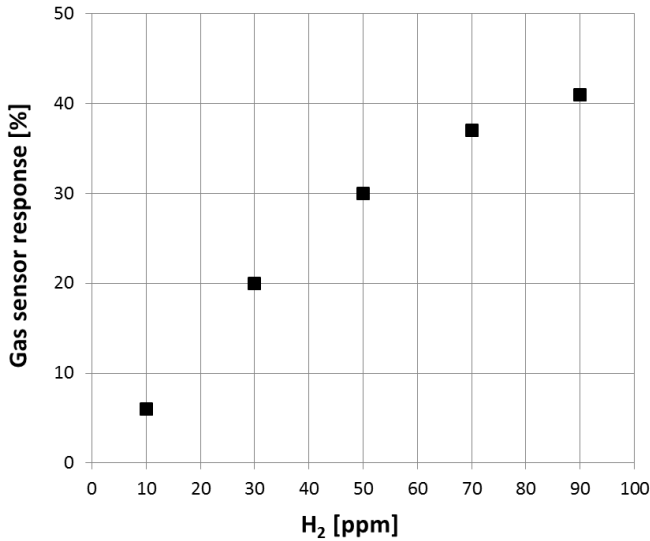


Fig. 4. Gas sensor response (%) for varying concentrations of H₂ gas in a humid synthetic air (RH=40%) environment. The sensing temperature is set to 350°C.

Set method is utilized in order to describe the top surface of a semiconductor wafer as well as the interfaces between different materials. The Level Set method describes a movable surface $\mathcal{S}(t)$ as the zero Level Set of a continuous function $\Phi(\vec{x}, t)$ defined on the entire simulation domain,

$$\mathcal{S}(t) = \{\vec{x} : \Phi(\vec{x}, t) = 0\}. \quad (1)$$

The continuous function $\Phi(\vec{x}, t)$ is obtained using a signed distance transform

$$\Phi(\vec{x}, t = 0) := \begin{cases} -\min_{\vec{x}' \in \mathcal{S}(t=0)} \|\vec{x} - \vec{x}'\| & \text{if } \vec{x} \in \mathcal{M}(t = 0) \\ +\min_{\vec{x}' \in \mathcal{S}(t=0)} \|\vec{x} - \vec{x}'\| & \text{else,} \end{cases} \quad (2)$$

where \mathcal{M} is the material described by the Level Set surface $\Phi(\vec{x}, t = 0)$. The implicitly defined surface $\mathcal{S}(t)$ describes a surface evolution, driven by a scalar velocity $V(\vec{x})$, using the Level Set equation

$$\frac{\partial \Phi}{\partial t} + V(\vec{x}) \|\nabla \Phi\| = 0. \quad (3)$$

In order to find the location of the evolved surface, the velocity field $V(\vec{x})$, which is a calculated scalar value, must be found.

The Level Set equation can be solved using numerical schemes developed for the solution of Hamilton-Jacobi equations, since the Level Set equation belongs to the class of Hamilton-Jacobi equations, given by

$$\frac{\partial \Phi}{\partial t} + H(\vec{x}, \nabla \Phi, t) = 0 \text{ for } H(\vec{x}, \nabla \Phi, t) = V(\vec{x}) \|\nabla \Phi\|, \quad (4)$$

where H denotes the Hamiltonian. The Level Set equation can then be solved using finite difference schemes such as the Euler method [24], the Upwind scheme, based on the Engquist-Osher scheme [25], or the Lax-Friedrichs Scheme for non-convex Hamiltonians [26]. Another advantage of using the Level Set method is that calculations of geometric variables such as the surface normal or the curvature are available directly from the implicit surface representation.

II. SPRAY PYROLYSIS DEPOSITION

During the last several decades, coating technologies have garnered considerable attention, mainly due to their functional advantages over bulk materials, processing flexibility, and cost considerations [27]. Thin film coatings can be deposited using physical methods or chemical methods. The chemical methods can be split according to a gas phase deposition or a liquid phase deposition. These processes are summarized in Fig 5, where chemical vapor deposition (CVD) and Atomic Layer Epitaxy (ALE) are the gas processes.

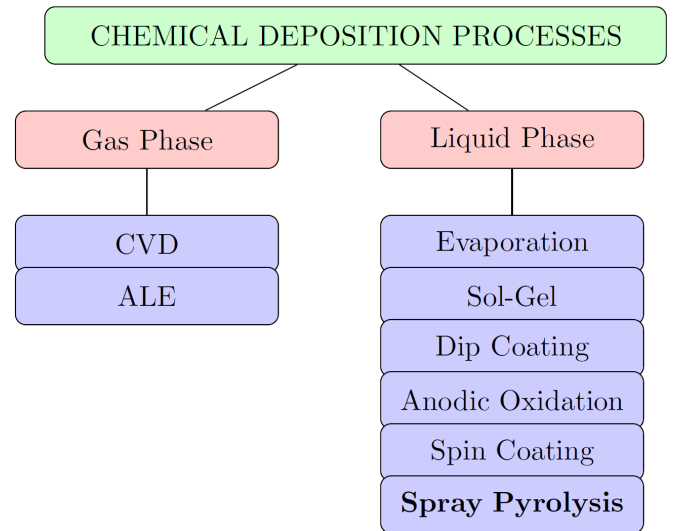


Fig. 5. Summary of chemical thin film deposition techniques.

Spray pyrolysis, as can be seen in Fig 5, is a technique which uses a liquid source for thin film coating. The first introduction of the spray pyrolysis technique by Chamberlin and Skarman [28] in 1966 was for the growth of CdS thin films for solar cell applications. Since then, the process has been investigated with various materials, such as SnO_x [29], In₂O₃ [30], Indium Tin Oxide (ITO) [31], PbO [32], ZnO [33], ZrO₂ [1], YSZ [34] and others [35].

The main advantages of spray pyrolysis over other similar techniques are:

- Cost effectiveness.
- Possible integration after a standard CMOS process.
- Substrates with complex geometries can be coated.
- Relatively uniform and high quality coatings.
- No high temperatures are required during processing (up to ~400°C).
- Films deposited by spray pyrolysis are reproducible, giving it potential for mass production.

The major interest in spray pyrolysis is due to its low cost and ease of incorporation within a standard CMOS process flow. It is used for the deposition of a transparent layer on glass [36], the deposition of a SnO₂ layer for gas sensor applications [29], the deposition of a YSZ layer for fuel cell applications [34], anodes for lithium-ion batteries [37], and optoelectronic devices [38].

The general simplified scheme for spray pyrolysis deposition is shown in Fig 6, where three processing steps can be viewed and analyzed:

- 1) Atomization of the precursor solution as it is pushed out of the atomizer.

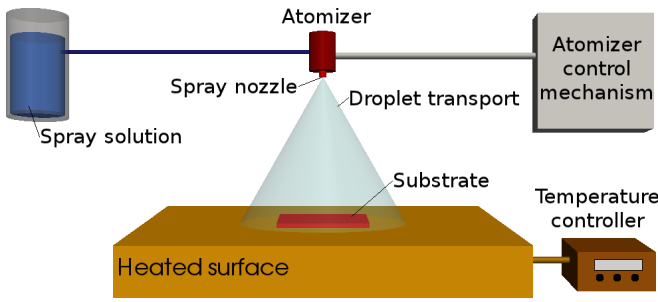


Fig 6. General schematic of a spray pyrolysis deposition process.

- 2) Aerosol transport of the droplet towards the substrate under the influence of external forces.
- 3) Droplet evaporation, spreading on the substrate, and drying and decomposition of the precursor salt to initiate film growth.

These three steps are individually addressed in the sections to follow.

III. PROCESS SEQUENCE DURING DEPOSITION

A. Precursor Atomization

The atomization procedure is the first step in the spray pyrolysis deposition system. The idea is to generate droplets from a spray solution and send them, with some initial velocity v_0 and radius r_d , towards the substrate surface. Spray pyrolysis normally uses air blast, ultrasonic, or electrostatic techniques [39]. The atomizers differ in resulting droplet size, rate of atomization, and the initial velocity of the droplets. For electrical atomizers, it has been shown that the size of the generated droplet is not related to any fluid property of the precursor solution and depends solely on the fluid charge density level ρ_e as shown in [40]

$$r^2 = \left(\frac{-\alpha'}{\beta'} \right) \frac{3\epsilon_0}{q\rho_e}, \quad (5)$$

where ϵ_0 is the electrical permittivity, q is the elementary charge, and $-\alpha'/\beta'$ is a constant value equal to $\sim 1.0 \times 10^{-17} \text{J}$. When no electrical force is present and a fluid exits through a thin circular outlet, the radius of the droplets is given by [41]

$$r = \left(\frac{3r_n \gamma_d}{2\rho_d g} \right)^{1/3}, \quad (6)$$

where r_n is the outlet radius, ρ_d is the droplet density, and γ_d is the droplet surface tension. When we analyze (6), it is evident that the only variable which can easily be modified to decrease the generated droplets is the circular outlet radius r_n . This is a significant limitation, since there are manufacturing limitations which restrict the size reduction of the outlet radius. In order to overcome this limitation it can be noted that, although the force of gravity can not be altered, an additional force can be used to push the liquid through the opening, resulting in an increase in effective g from (6). This effect is governed by the critical Weber number

$$W_{crit} = \frac{2\rho_a v_{rel}^2 r}{\gamma_d}, \quad (7)$$

where ρ_a is the air gas density, v_{rel} is the relative velocity. The critical Weber number has a value of 22 for a free falling

droplet and 13 for a droplet which is suddenly exposed to a high velocity [42]. Therefore, a sudden increase in the droplet's velocity will result in that droplet splitting into multiple droplets with a reduced radius. This is the main concept behind air pressure atomizers. An added compressed gas (N_2) is introduced into the atomizer; increasing the pressure of the gas causes an increased velocity of the exiting fluid and thereby smaller droplet radii.

The mass of a droplet, assuming a spherical shape depends on its density

$$m = \frac{4\pi}{3} \rho_d r^3, \quad (8)$$

where r is the droplet radius. The initial leaving velocity of the droplet is an important parameter as it determines the rate at which the droplets reach the substrate surface, the heating rate of the droplet, and the amount of time the droplet remains in transport the spray pyrolysis environment. Table I summarizes the properties of droplets for different atomizers commonly used for spray pyrolysis deposition.

Table I
CHARACTERISTICS OF ATOMIZERS COMMONLY USED FOR
SPRAY PYROLYSIS.

| Atomizer | Droplet diameter (μm) | Droplet velocity (m/s) |
|---------------|------------------------------------|------------------------|
| Pressure | 5 - 50 | 5 - 20 |
| Ultrasonic | 1 - 100 | 0.2 - 0.4 |
| Electrostatic | 5 - 70 | 1 - 4 |

The ultrasonic nozzles apply a relatively small amount of energy and can produce droplets with a radius down to approximately $2\mu\text{m}$, but at the cost of a low atomization rate ($< \sim 2\text{cm}^3/\text{min}$) [1]. Due to its ease of production, many companies chose to use pressure atomizers instead of the ultrasonic atomizers. This work will mainly concern itself with the pressure and electrostatic atomizers, characterized in further detail in [29] and [39], respectively.

A pressure, or air blast, atomizer uses high speed air in order to generate an aerosol from a precursor solution. Increasing the air pressure causes a direct decrease in the generated mean droplet diameter. Inversely, increasing the liquid pressure causes a direct increase in the mean droplet diameter [43]. Increasing the distance between the spray nozzle and the surface to be coated reduces the heating effect, resulting in a reduced deposition rate, but an increased coating area. Another way to achieve the same effect is to increase the spray angle of the nozzle in use. Perednis [3] showed that all droplets sprayed from an air blast atomizer are contained within a 70° spray cone angle, while half are within a narrower 12° angle. It was also determined that the flow rate has a very small influence on the spray characteristics, which can be mostly ignored during modeling.

B. Aerosol Transport of Droplets

After the droplet leaves the atomizer, it travels through the ambient with an initial velocity determined by the atomizing nozzle. In the aerosol form, the droplets are transported with the aim of as many droplets as possible reaching the surface. As the droplets move through the ambient, they experience the physical and chemical changes depicted in Fig 7.

As the droplet traverses the ambient, there are four forces simultaneously acting on it, describing its path. Those forces

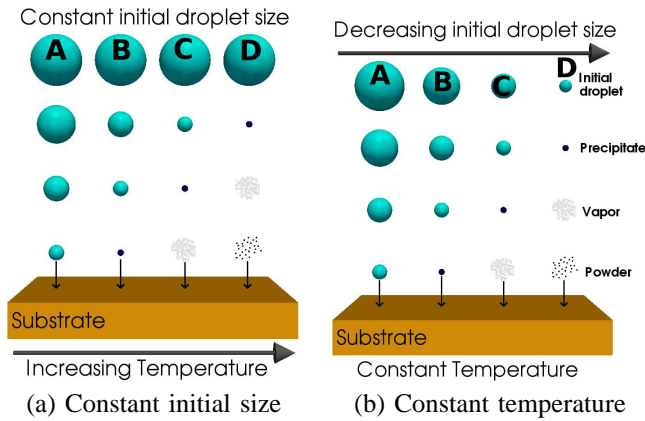


Fig 7. Spray pyrolysis droplets modifying their physical and chemical properties as they are transported from the atomizing nozzle to the substrate. Whether the temperature [44] or the initial droplet size [45] are varied, there are four potential modification paths which the droplet can take as it moves towards the substrate (A-D).

are gravitational, electrical, thermophoretic, and the Stokes force. As shown in Fig 7, the droplets experience evaporation during their flight, which affects the influence of the forces on their trajectory. Some experimental results from [46] indicate that solid particles could form, when the reactor temperature is low, when the precursor solution concentration is high, and when the flow rate of the carrier gas (N_2) is low. The forces of influence to the transport are further analyzed in the sections to follow.

1) *Gravitational force*: The gravitational force is the force pulling the droplet downward. The size of the force depends on the mass of the traveling droplet, given by (8). The gravitational force is a function of its volume and its density. The force is given by

$$F_g = \frac{4\pi}{3} \rho_d r^3 g, \quad (9)$$

where ρ_d is the density of the droplet and g is the acceleration due to gravity. For small droplets the force of gravity is too small to allow it to arrive at the surface before it is fully evaporated and converted into a powder. For larger particles, the force of gravity is the driving force behind the droplet transport.

2) *Electrical force*: The electrical force is applicable to spray pyrolysis systems which include an additional electrical source governing the droplet's trajectory. When an air blast atomizer is used, high speed air and an additional gas pressure such as N_2 are the causes of atomization and aerosol production. Ultrasonic atomizers are electrically driven, whereby an electric generator is vibrated at ultrasonic frequencies through a titanium nozzle. Increasing the frequency can result in smaller droplet sizes. Electric spray deposition (ESD) atomizers use a strong electric field at the liquid-gas interface to generate charged droplets. Therefore, air blast atomizers do not have additional contributions from an electrical force and the droplet transport is driven by the gravitational force and the initial velocity, while for spray pyrolysis deposition using ultrasonic and ESD atomizers, the electrical force is the main component which drives the droplets downwards. The electrical force acting on a droplet is usually several orders of magnitude larger than

the gravitational force [34] and is given by

$$F_e = q_d E, \quad (10)$$

where E is the generated electric field strength and q_d is the droplet charge. The droplet charge q_d is dependent on the temporal change of the droplet and is given by

$$q_d = q_{max} \frac{t}{t + t_0} \quad (r \gg 1\mu m), \quad (11)$$

with

$$q_{max} = 8\pi\sqrt{\gamma\epsilon_0}r^3 \quad \text{and} \quad t_0 = \frac{4}{b \operatorname{div}E}, \quad (12)$$

where γ is the liquid-gas surface tension and b is the ionic mobility [45].

3) *Stokes force*: The Stokes force is the drag experienced by the droplet due to the air resistance in the ambient. The force is caused by the friction between the droplet and air molecules. The Stokes force is a factor of the particle's velocity and volume. Therefore, large droplets which move with a high velocity will experience the largest retarding Stokes force according to

$$F_S = 6\pi\eta_a r (v_d - v_a) \left(1 + \frac{3}{8}\operatorname{Re}\right), \quad (13)$$

where η_a is the viscosity of air, v_d is the droplet velocity, v_a is the air velocity, and Re is the Reynolds number. For spherical particles, the Reynolds number is given by

$$\operatorname{Re} = \frac{2r(v_d - v_a)\rho_a}{\eta_a}, \quad (14)$$

where ρ_a is the density of air. Because the $\frac{3}{8}\operatorname{Re}$ term in (13) is very small ($\frac{3}{8}\operatorname{Re} \ll 1$), it is often excluded from Stokes force calculations.

4) *Thermophoretic force*: Similar to the Stokes force, the thermophoretic force is a retarding force, causing droplets to significantly decrease their velocity as they approach the heated substrate. Fig 8 shows the temperature distribution near a heated substrate. The results for the 400°C sample are measured and they show how the air temperature varies away from the heated surface. It is evident that the air temperature increases steeply due to the forced convection cooling effect of the air flow when close to the heated substrate, resulting in a high thermal gradient of approximately $30^\circ\text{C}/\text{mm}$. Because the thermophoretic force depends on the thermal gradient in the transport environment, it can be concluded that it will have no effect on the droplet movement, when it is more than several (~ 7) mm away from the substrate. However, in this high thermal gradient region, the thermophoretic force begins to dominate. This is true for pressure spray deposition (PSD) systems where the main driving force is gravity; however, for ESD systems, the electrical force is often stronger than the thermophoretic force [3]. The increased temperature has additional effects on the droplet, such as a reduction in its size due to droplet evaporation in the region.

The equation governing the strength of the thermophoretic force is given by

$$F_t = \frac{3\pi\eta_a^2 r}{\rho_a} \cdot \frac{3\kappa_a}{2\kappa_a^2 + \kappa_d} \cdot \frac{\nabla(T_a)}{T_a}, \quad (15)$$

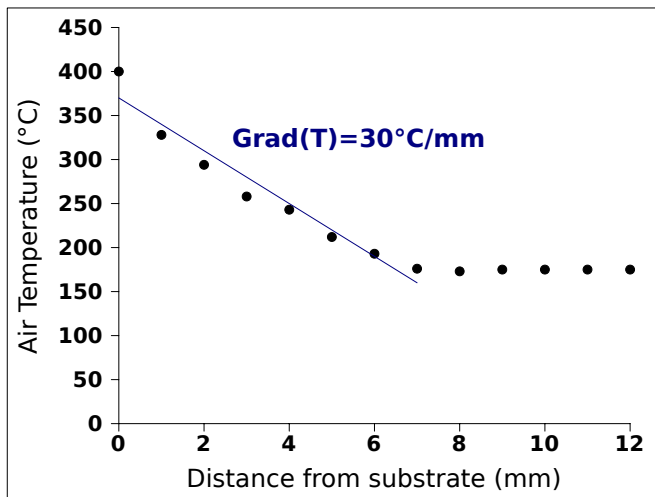


Fig 8. Air temperature above a heated plate for a substrate temperature of 400°C during a pressurized spray process.

where η_a is the viscosity of air, T_d is the droplet temperature, T_a is the air temperature, ρ_a is the density of the air, and $\nabla(T_d)$ is given by

$$\nabla(T_d) = \frac{3\kappa_a}{2\kappa_a^2 + \kappa_d} \cdot \nabla(T_a), \quad (16)$$

where κ_a and κ_d are the thermal conductivities of the air and the droplet, respectively. It should be mentioned that (15) is only valid for droplets whose radius is much larger than the mean free path of the air molecules.

C. Precursor Decomposition

The precursor, as it moves through the heated ambient undergoes various changes, which are characterized in Fig 7. Evaporation, precipitate formation, and vaporization all occur depending on the droplet size and ambient temperature. The four processes (A–D) from Fig 7 show the four physical forms in which the droplet may interact with the substrate surface. Although all processes occur during deposition, Process C, the CVD-like deposition is desired to yield a dense high quality film [3].

1) Process A: low temperature - large initial droplet:

When the large droplets approach a heated substrate and the temperature is not sufficiently high to fully evaporate the solution, they will impact with the substrate and decompose. Upon contact, the droplet is entirely vaporized and a dry precipitate is left behind. Because droplet vaporization requires some heat, the substrate temperature is slightly decreased at the impact point, adversely affecting the reaction kinetics [45]. This process has a weak sticking probability.

2) Process B: lower/intermediate temperature - larger/medium droplet size:

When medium-sized droplets are initially formed, some evaporation occurs. Just as the droplet reaches the surface, however, it forms a precipitate as an amorphous salt and a dry precipitate hits the surface, where decomposition occurs. Some particles evaporate and condense into gaps between particles, where surface reaction occurs. However, this process has a medium sticking probability.

3) *Process C: intermediate/higher temperature - medium/smaller droplet size:* When the processing environment causes droplets to evaporate prior to reaching the substrate vicinity, a precipitate will form early. As the precipitate reaches the immediate vicinity of the substrate, it is converted into a vapor state and it undergoes a heterogeneous reaction through the following steps [45]:

- 1) Reactant molecules diffuse to the surface.
- 2) Adsorption of some molecules at the surface.
- 3) Surface diffusion and a chemical reaction, incorporating the reactant into the lattice.
- 4) Desorption and diffusion of the product molecules from the surface.

This is a classical CVD reaction, which results in a high quality film deposition and a high sticking probability.

4) Process D: high temperature - small droplet size:

When small initial droplets are formed, or the temperature is high enough, the droplet quickly forms a precipitate. As the precipitate approaches the substrate, it is vaporized and a chemical reaction subsequently occurs in the vapor phase. This homogeneous reaction leads to the condensation of molecules into crystallites in the form of a powder precipitate. The powder falls to the substrate surface, but without a deposition reaction.

IV. MODEL I – DROPLET TRANSPORT

Forces acting on the droplet can be calculated and applied to droplets in order to find the location where the droplet makes impact with the surface. This is a challenge because the simulation environment must now be divided into several segments. The first segment which must be treated separately is the thermal zone which is within 10mm of the wafer surface. In this area, the temperature gradient shown in Fig 8 is high and the thermal force plays a significant role in the droplet speed as well as size, due to evaporation. In addition, when the electrical force is included, the complexity of the problem is significantly increased, since this force is position-dependent.

Fig 9 shows how the simulation space is divided in order to accommodate the thermal zone for droplets. A detailed derivation of the droplet transport equations can be found in [47] as well as in Appendix I and Appendix II.

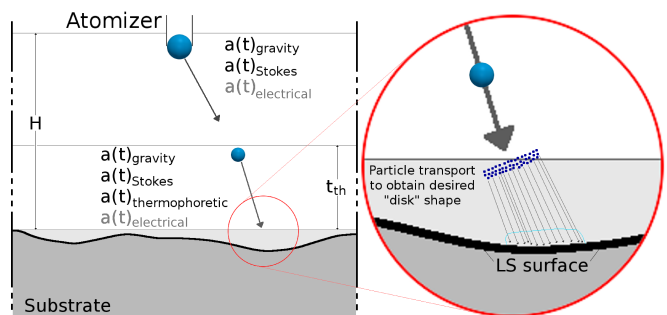


Fig 9. The droplet transport in the space above the substrate surface and the accelerations which are considered in the transport model. t_{th} is the height of the thermal zone ($\sim 10\text{mm}$ for ESD, $\sim 5\text{mm}$ for PSD), and H is the distance between the substrate and atomizer.

A. Droplet Atomization

The first step in the model is finding the droplet size as it exits the atomizer. The distribution of droplet sizes does not follow any standard distribution, but it is suggested that the volume fraction varies relatively evenly near the approximate value 0.05 for droplets between with a radius between $2.5\mu\text{m}$ and $55\mu\text{m}$ [3], [48]. Therefore, the distribution for the droplet radii is simulated by generating an even distribution for the volume fraction ξ_{vol} followed by finding the radius distribution for the droplet r_d : Droplets with a radius below $2.5\mu\text{m}$ are ignored, because they are not expected to take part in the deposition reaction. The distribution of the droplet's radius is derived in Appendix III and is given by

$$r_d = \left\{ \xi \cdot \left[(r_{max})^{-1/3} - (r_{min})^{-1/3} \right] + (r_{min})^{-1/3} \right\}^{-3}, \quad (17)$$

where $r_{min} = 2.5\mu\text{m}$ and $r_{max} = 55\mu\text{m}$ are the minimum and maximum radii for the generated droplets and $\xi \in [0, 1]$ is an evenly distributed random value.

B. Droplet Acceleration due to External Forces

In order to follow the trajectory of a droplet after leaving the atomizer and under the influence of gravity, Stokes, electric, and thermophoretic forces, the distance required for the droplet to travel $d(t)$, the initial velocity v_0 , and the droplet radius r_d are known. Although the thermophoretic force does not affect the droplet motion until it reaches the vicinity of the wafer, it will be included in the derivation of the equations of motion. This allows for the most complex system to be solved, which includes all forces.

Given the four forces discussed previously, the acceleration experienced by the particle is given by

$$a(t) = g - l + s v(t) + c d(t), \quad (18)$$

where g and l are accelerations caused by the gravitational and thermophoretic forces, respectively. Acceleration s is a velocity-dependent parameter and is caused by the Stokes force, while c is the simplified linearized displacement-dependent acceleration due to the electrical force where

$$l = \frac{27 \eta_a^2 \kappa_a \nabla(T_a)}{4 \rho_a \rho_d T (2\kappa_a + \kappa_d) r_d^2}, \quad \text{and} \quad s = \frac{9 \eta_a}{2 \rho_d r_d^2}. \quad (19)$$

For the purposes of a topography simulation, an assumption for a constant electric field is sufficient [3]. Because the electrical force factor, c from (18), can only be introduced into the model in the form of linear simplifications, special attention is paid to its implementation. The first step is to connect the generated electric field to the fitting variable c .

$$c = \frac{6}{\rho_d} \sqrt{\frac{\gamma \epsilon_0}{r_d^3}} \cdot \frac{\Phi_0}{H} \cdot \frac{K_V}{\log(4H/R)} c_e \quad (20)$$

where Φ_0 is the applied electrical potential, H is the distance between the nozzle and substrate, R is the outer radius of the nozzle, and K_V is a value which ranges from 0 to 1 depending on the H/R ratio [49]. The variable c_e is a linearization constant which represents a best-fit to the normalized electric field in the region.

Fig 10 shows the value for the normalized potential $\Phi^* = \Phi/\Phi_0$ and its distribution in an ESD deposition setup. The atomizing nozzle is located at $(0, 1)$. The inset shows the

electric field distribution in the same simulation space. It is evident that the strength of the electric field is not uniform or linear, but that the field causes charged droplets to spread radially.

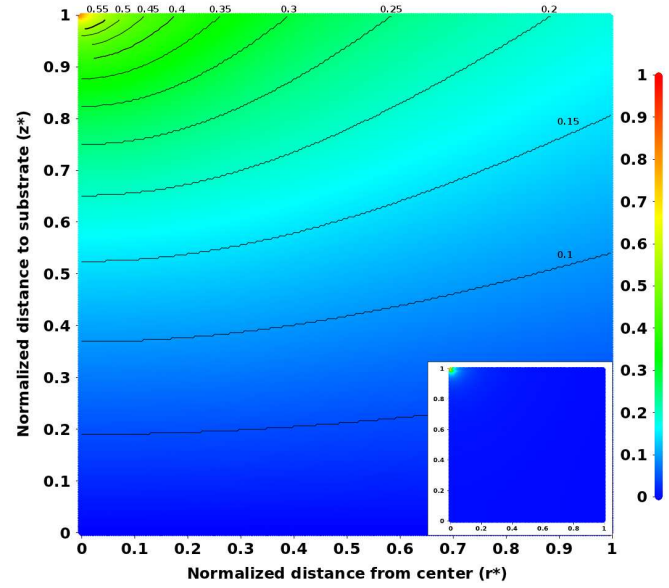


Fig 10. Magnitude of the normalized electric potential Φ/Φ_0 during ESD processing. The distance between needle and deposition plate as well as the radial distance from the center are normalized to the distance between the atomizer and the substrate. The inset is the normalized electric field distribution.

For the purposes of spray deposition, it is often assumed that the value of K_V is 1, because the ratio of H/R is on the order of several hundreds, which gives a value close to 1 for K_V . However, after some calculations, it was found that the value of K_V is better represented using the relationship

$$K_V = 1 - e^{-0.021 \frac{H}{R}}, \quad (21)$$

which is implemented in our model. In fact, assuming that $K_V = 1$ can cause erroneous results for the electric field. The negative exponential dependence on R from (21) is in the numerator of c from (20), which shows an additional inverse logarithmic dependence in the denominator. A plot of the fraction $K_V / [\log(4H/R)]$ for various R values is shown in Fig 11, when the variation in K_V is taken into account and when it is assumed that $K_V = 1$. It is clear that the effects of K_V should be included in the droplet transport model when $R/H > 0.005$.

The droplets trajectory is tracked by applying two systems of equations. The first system calculates the length of time required for the droplet to overcome the vertical displacement required to be on the same plane as the wafer surface. This means that the vertical displacement is known and the time required to reach it must be found. The second system uses the calculated time for the droplet's vertical flight in order to determine the radial location of the droplet's final position.

1) *Vertical transport of droplets:* The full set of equations and derivations for the time required for a droplet to reach a desired displacement under the influence of velocity- and displacement-dependent forces is shown in Appendix II. Here, the result of that derivation is shown, which is implemented in the model. Note that the subscript v in the following equations refers to the vertical component of the

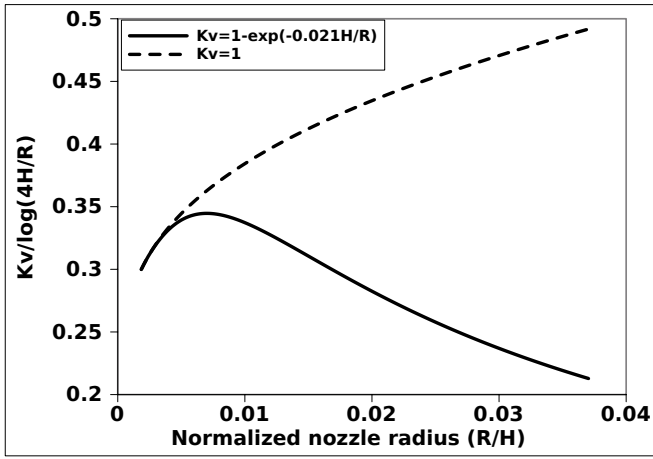


Fig 11. The effects of varying the atomizing nozzle's outer radius on the strength of the electric field with and without the K_V effects.

given variable. The initial droplet velocity has a vertical v_{0v} and radial v_{0r} component. The droplet displacement resulting from the acceleration given in (18)-(20) is given by

$$d_v(t) = C_1 e^{-r_1 t} + C_2 e^{-r_2 t} + C_3, \quad (22)$$

where

$$r_1 = \frac{-s + \sqrt{s^2 - 4c}}{2}, \quad r_2 = \frac{-s - \sqrt{s^2 - 4c}}{2}, \quad (23)$$

and

$$\begin{aligned} C_1 &= r_1 v_{0v} - \frac{r_1^2 r_2}{r_1 - r_2} \left[(g - l) - v_{0v} \left(\frac{1}{r_1} + s \right) \right], \\ C_2 &= \frac{r_1 r_2^2}{r_1 - r_2} \left[(g - l) - v_{0v} \left(\frac{1}{r_1} + s \right) \right], \\ C_3 &= \frac{c}{1 + (g - l) + s}. \end{aligned} \quad (24)$$

Inverting (22) to find the time required for the droplet to reach the known displacement d_v is quite complex and must be solved iteratively. However, when the electrical force is not included in the equations, then the displacement, calculated in the previous section of Appendix I, becomes

$$d(t) = \frac{1}{b} \left(v_0 - \frac{a}{b} \right) (1 - e^{-bt}) + \frac{a}{b} t. \quad (25)$$

Inverting (25) to find the time t , we obtain

$$t = \frac{g W[\mathcal{Z}] - g + s v_{0v} + s^2 d_v}{g s}, \quad \text{where} \quad (26)$$

$$\mathcal{Z} = \frac{(g - s v_{0v}) \cdot e^{\frac{1 - s(v_{0v} + s d_v)}{g}}}{g}.$$

$W[\cdot]$ is the Lambert-W function defined by

$$z = W(z) e^{W(z)}. \quad (27)$$

An explicit equation for the time required to achieve the displacement in (22) cannot be found. Therefore, the droplet motion is solved by time discretization, Monte Carlo methods, or iteratively in order to obtain the droplet trajectory through the electric field. An iterative solver is implemented within the simulator, which solves the Lambert function [50].

After finding the time required for the droplet to reach the height of the wafer surface, a similar derivation can be used to find the radial location of the droplet using the vertical flight time. It is also important to note that the full extent of the radial distance need not be incorporated in the linearization process. When considering the deposition on a chip which extends 1mm radially from a spray source located at a vertical distance of 100mm, this means the radial distance $R \leq 0.01$ is of importance.

2) *Radial transport of droplets:* In order to calculate the radial trajectory, the time t , the droplet radius r_d , and the initial radial velocity v_{0r} must be known. The time parameter is derived using the vertical trajectory discussion. The electrical force is only applicable to vertical motion since this is how the electric field appears to the droplets in the very thin region of interest between the nozzle and wafer surface. The force of gravity does not influence the radial movement of the droplet as well. Therefore, only the Stokes force must be considered. Note that the subscript r in the following equations refers to the vertical component of the given variable. The acceleration of the droplet is defined as

$$a_r(t) = -\frac{9\eta_a}{2\rho_d r_d^2} v_r(t) \quad \text{or} \quad a_r(t) = -s v_r(t) \quad (28)$$

Similar methods used for the vertical trajectory can be used to solve the radial velocity given by

$$v_r(t) = v_{0r} e^{-st} \quad (29)$$

and the radial displacement

$$d_r(t) = \frac{v_{0r} (1 - e^{-st})}{s}. \quad (30)$$

The vertical and radial location as well as the velocity of the droplet is now known. The radius remains unchanged, as it was experimentally shown that the droplet radius is largely unaffected outside of the heat zone [3]. The droplet carries information regarding its position, velocity, and radius as it passes to the next step in the model. Within the heat zone, where the thermophoretic force is also present, the droplet radius is reduced and the calculations are repeated until a vertical displacement is sufficient for the droplet to traverse the thermal region and reach the surface of the wafer.

C. Modeling Interaction between Droplet and Wafer Surface

For the droplet transport model, the deposition is carried out by analyzing the influence of individual droplets. As each droplet reaches the wafer surface, it spreads into a disk-like shape, resulting in overlapping disks on the surface. This interaction assumes the combination of a sufficiently-large droplet volume and weak retardant forces when compared to the electrical force. Within the Level Set code, the disk shapes are generated by evenly distributing multiple particles, representing each droplet, in a circular pattern around the point of impact between the droplet and surface. The thickness and radius of the deposited disk depends on the individual droplet volumes.

V. MODEL II – DEPOSITION OF VAPOR

A. Experimental Setup

The deposition of tin oxide (SnO_2) on silicon dioxide using the spray pyrolysis deposition process was performed

using an air atomizer which is not located directly above the wafer, but rather on the side, emitting a spray towards the wafer. as depicted in Fig 12.

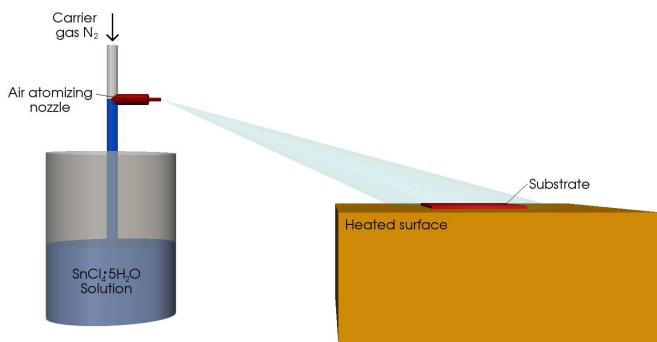


Fig 12. Schematic for the spray pyrolysis process used at AIT, serving as a basis for the presented topography simulations.

Additionally, the nitrogen pressure of the atomizer was set to 2bar in air and 0.7bar in the liquid. These values are outside of the data sheet for the nozzle used [43], which is done in order to obtain smaller droplet sizes and slower deposition rates [22]. However, the data sheet information was extracted and the provided graph extended in order to find an approximate radial distribution of particles. The droplet radii vary between $1.5\mu\text{m}$ and $5.5\mu\text{m}$. The spray direction is also extrapolated from the data sheet for the simulation.

The spray nozzle in use is one which produces a flat spray pattern with droplet dispersal proceeding mainly in the lateral axial direction. The vertical direction experiences much less particle dispersal; however, some dispersal does occur and the ratio between the lateral and vertical dispersal is approximated to 10:1. The nozzle is approximately 20cm laterally and 10cm vertically distanced from the substrate and the spray is directed such that much of it is found above the heated surface, where it can deposit onto the wafer. The initial velocity of the droplets, as they are pushed out of the atomizer are approximations made based on values found in literature which suggest an initial particle velocity between 5m/s and 20m/s.

In the experimental setup the lack of a strong electrical force and the very small size of droplets results in the droplets not being able to be simulated individually, but that interactions between droplets during their flight plays a significant role in their trajectory. As the droplets reach the surface, their small size causes them to evaporate in the near vicinity of the heated wafer and deposit in the manner of a vapor deposition.

B. Experimental Observation

There are several factors which influence the final thickness of the deposited film. Those include spraying time, volume of the sprayed solution, air pressure, distance of the atomizer from the substrate, temperature of the pyrolysis reaction, and time of the solution (SnCl_4) aging. It was found in [29] that thicknesses of the deposited SnO_2 film decrease, when the time interval between its preparation and its use in the pyrolysis reaction increases. A suggestion is made to use either a freshly made solution or a completely aged solution during spray pyrolysis. During the presented experiments, the

the nozzle distance to the substrate, the air pressure, and the solution aging remain constant, while the spray is constantly applied.

After performing spray pyrolysis deposition, while directing the spray in parallel and perpendicular to the electrodes as depicted in Fig 13, the V-I curves of the two chips are

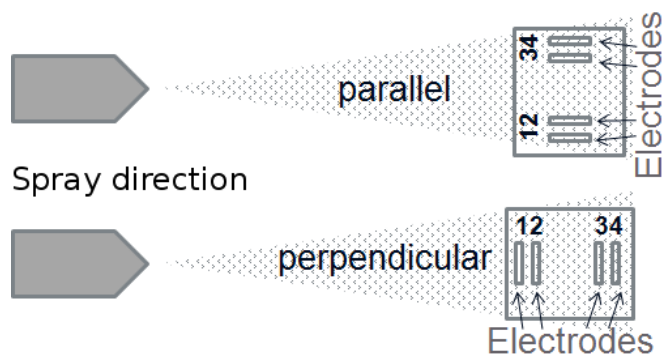


Fig 13. Spray direction during deposition.

visualized in Fig 14. It was noted that regardless of the initial spray direction and the direction of the droplets as they leave the atomizing nozzle, the thickness of the grown thin film and its electrical properties remain unchanged.

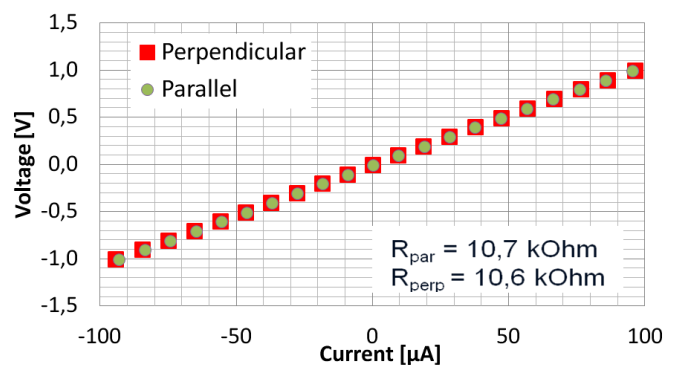


Fig 14. V-I curves between Electrode 1 and Electrode 4 for the chips depicted in Fig 13.

This is likely due to the nozzle being placed at a distance of approximately 30cm away from the substrate surface, giving enough time for the Stokes retardant force to effectively remove any influence of the droplets' initial horizontal velocity. Therefore, directionality plays no role in the film deposition process. This also helps to eliminate the potential of large droplets splashing onto the substrate surface. Large droplets generally do not deposit uniformly on the desired surface, but rather impact the heated wafer while in liquid form, leaving behind a powder residue with weak sticking properties to the silicon. The large droplets experience a higher Stokes retardant force causing them to never reach the 30cm displacement between the particle generation and the substrate surface location.

The thickness of the tin dioxide layer depends on the spray temperature and the spray time. With the heatpad temperature set to 400°C , the thickness of the SnO_2 layer is plotted against the spray time in Fig 15. A linear relationship is evident.

The thickness of the grown film does not change when the deposition takes place on a step structure, as shown

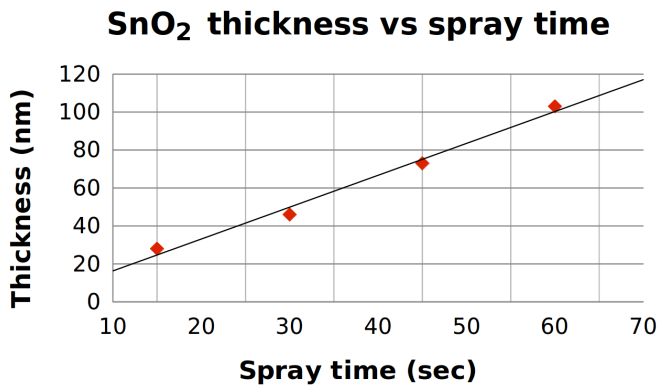


Fig 15. The influence of spray time on the thickness of the deposited SnO₂ layer, with temperature set to 400°C.

in Fig 16(a), suggesting that the deposition is a result of a CVD-like process and not a process which alludes to a direct interaction between the deposition surface and the liquid droplets. Fig 16(a) shows a resulting SnO₂ thin film after a spray pyrolysis deposition step lasting 45 seconds with the substrate heated to 400°C. The resulting film thickness is approximately 75–80nm. We conclude that the droplets, which carry the depositing material, interact with the substrate surface as a vapor and then deposit in a process analogous to CVD.

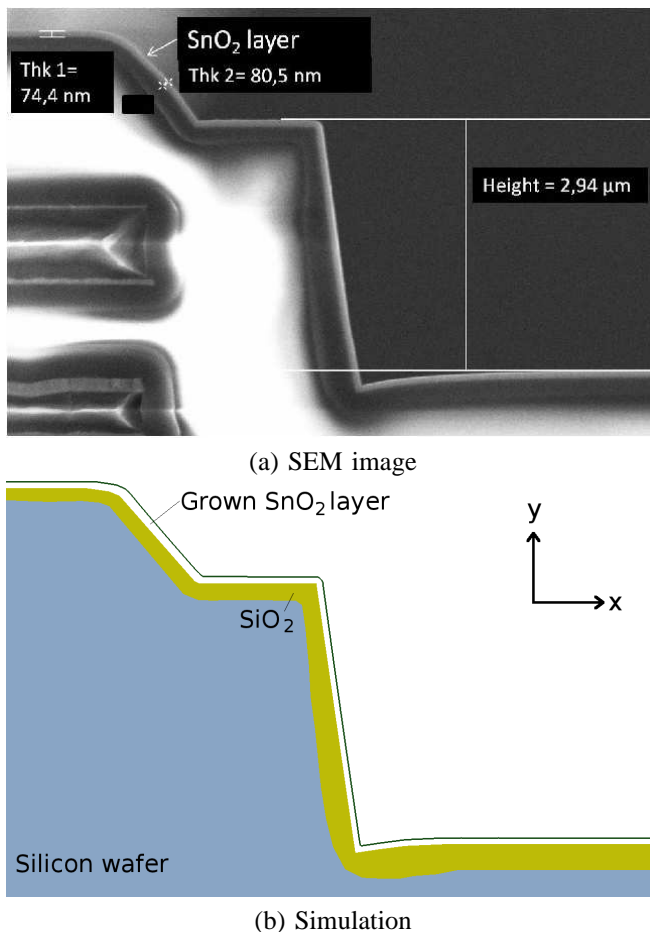


Fig 16. Images showing the deposited SnO₂ film as a results of a deposition step. The good step coverage confirms a chemical and not physical reaction takes place during deposition. The temperature used for the experiment is set to T=400°C and the time $t=45$ seconds

C. Model Implementation

Our experimental data suggest a linear dependence on spray time and a logarithmic dependence on wafer temperature for the growth rate of the deposited SnO₂ layer. A good agreement is given by the Arrhenius expression

$$d_{SnO_2}(t, T) = A_1 t e^{(-E/k_B T)}, \quad (31)$$

where $A_1 = 3.1 \mu m/s$, the thickness is given in μm , t is the time in seconds, T is the temperature in Kelvin, and E is $0.427 eV$. Fig 16 depicts the (a) experimental and the (b) simulated topography of a deposited SnO₂ film on a step structure after applying a PSD process for 45 seconds at 400°C.

The growth equation (31) relates the thickness of the deposited material to the applied time and temperature. However, this uniform growth is only valid for flat surfaces, while deep trenches and sharp corners need extra considerations. Since the droplets fully evaporate prior to depositing on the surface, a non-linear simulation model analogous to CVD is implemented. The implementation requires the combination of Monte Carlo methods within the Level Set framework. A single particle species is considered during deposition. As the simulation is initiated, multiple particles are generated in the simulation space with an average direction perpendicular to and moving towards the wafer. The particles are represented in terms of individual fluxes, given by

$$\Gamma_{src} = \Gamma_{src}(\vec{x}; \vec{w}, E) \quad \vec{x} \in \mathcal{P}, \quad (32)$$

where \mathcal{P} is the surface which divides the region above the wafer (reactor-scale) and the region comprising the wafer (feature-scale) while the flux of arriving particles Γ_{src} is described in terms of particles which are moving in direction \vec{w} arriving with an energy E per unit area. This energy E is dependent on the time and temperature of the simulation space, as it is the deciding factor in the speed of the film growth. The distribution of particles stems from the idea that their transport is characterized by the mean free path of a gas $\bar{\lambda}$ which, for our process is in the range of 9mm. In this range, the particle velocities follow the Maxwell-Boltzmann distribution and the flux has a cosine-like directional dependence

$$\Gamma_{src}(\vec{x}; q, \vec{w}, E) = F_{src} \frac{1}{\pi} \cos\theta, \quad \cos\theta = \vec{w} \cdot \vec{n}_{\mathcal{P}}, \quad (33)$$

where F_{src} is uniform and $\vec{n}_{\mathcal{P}}$ is the normal vector to \mathcal{P} pointing towards the wafer surface.

In the feature-scale region, particles may also be reflected from the wafer walls, modeled using a sticking coefficient, resulting in their deposition elsewhere on the wafer or them leaving the simulation space entirely. Reflected particles follow the Knudsen cosine law [51]. The total flux is then composed of source particles with flux Γ_{src} and re-emitted particles, which stick on recursive impact Γ_{re} . For the spray pyrolysis deposition process, it was found that a sticking coefficient of 0.01 has the best fit to experimental data and was therefore used for the model. The motion of reflected or re-emitted particles is then tracked with their sticking probability reduced after each surface impact. The tracking of a single particle is deemed concluded when its sticking probability reaches 0.1% of the original sticking coefficient.

VI. SPRAY PYROLYSIS DEPOSITION SIMULATIONS

A. YSZ Deposition using ESD Pyrolysis

The YSZ deposition using an ESD process from [3] is simulated using Model I discussed in Section IV. The parameters of the solution used and therefore, the properties of the droplets which are simulated are listed in the table from Appendix IV. The given equation for the electric field provides the magnitude at each location; however, in order to follow the droplet trajectory, the individual components of the electric field in each direction are required such that, in cylindrical coordinates, $\vec{E}_{ext} = (E_\rho, \varphi, E_z)$. The droplet angle φ is unaffected by the applied forces since they act only in the radial ρ and vertical z directions.

Fig 17 shows a silicon surface geometry which extends 50mm by 50mm after 1, 10, 20, 50, and 100 spray cycles with 100,000 droplets per cycle and the spray nozzle located 270mm above the surface.

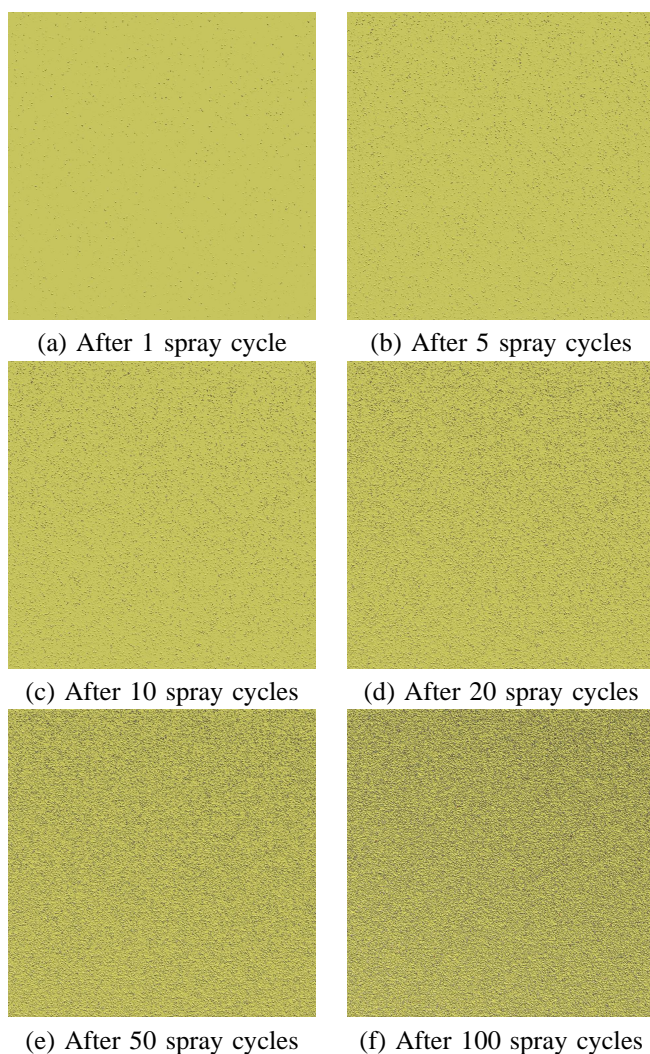


Fig 17. Macroscopic spray pyrolysis simulation on a 50mm by 50mm geometry. Each spray cycle contains 100,000 droplets.

The images in Fig 17 show little how the thin film is deposited, when the deposition process is modeled as a sequence of droplets landing onto the surface and depositing a disk shaped film. Fig 18 shows an area which expands 250 μ m by 250 μ m. Several droplets are shown including overlapping of the disk shapes on the surface as they are being deposited. The lighter surface is the wafer while the

darker disks are the deposited YSZ films. Each depositing droplet is modeled using 10^9 particles which accelerate to the surface and add a slight component to the overall deposited film thickness.

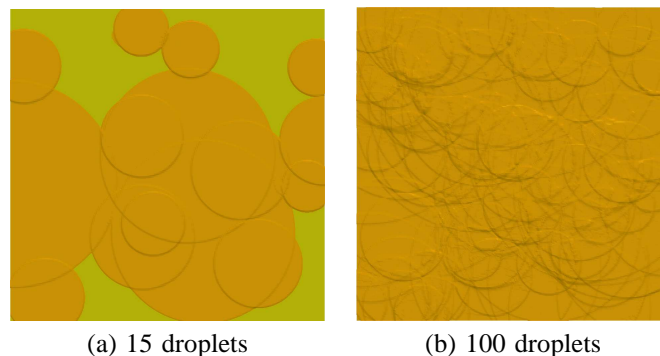


Fig 18. Spray pyrolysis simulation on a 250 μ m by 250 μ m geometry.

B. Tin Oxide Deposition using PSD Pyrolysis

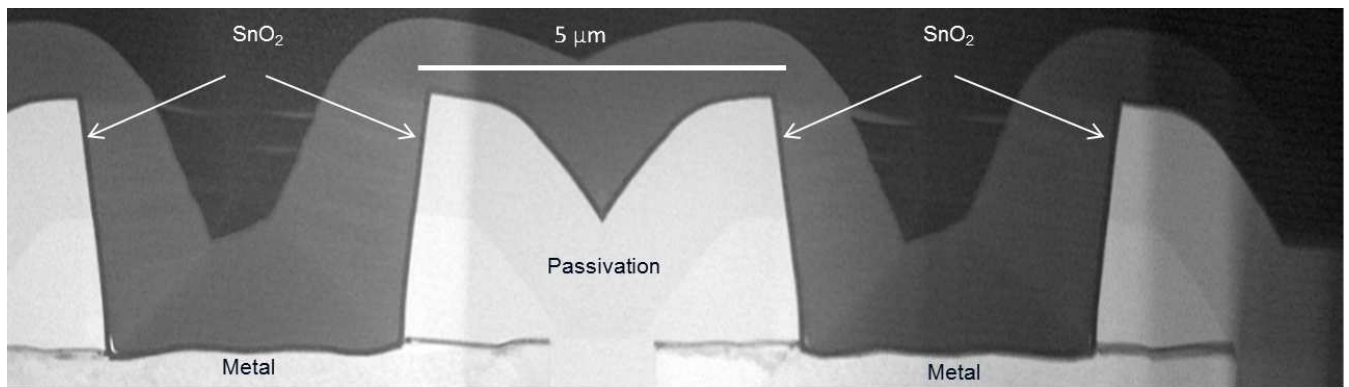
The presented simulations are performed using Model II, presented section V. The first simulation, shown in Fig 19(b) is compared to the measured result from Fig 19(a). The geometry is of a typical electrode structure for a SnO₂ gas sensor and is the front view for the FIB cut shown in Fig 2. The simulation and experiment is performed using a time of 30s and the substrate placed on a surface heated to 400 $^\circ$.

In order to observe how the deposition of SnO₂ films using spray pyrolysis fills various trench depths, several simulations are performed. The simulations were done on a trench with a 1000nm height and walls angled at 2 $^\circ$. A 30 second simulation at a temperature of 400 $^\circ$ C was carried out for trench widths of 300nm, 200nm, 150nm, 100nm, 75nm, and 50nm with results shown in Fig 20. The expected resulting SnO₂ thickness is 50nm. It is evident that when the trench width does not allow for the film to comfortably grow, a pinch-off at the top of the trench is visible. This is especially clear for the thinnest trenches of 75nm and 50nm in Fig 20(e) and Fig 20(f), respectively. In order to ensure a trench cavity large enough to enable the detecting gas to flow and be detected by the deposited layer, a minimum trench width of 200nm is recommended.

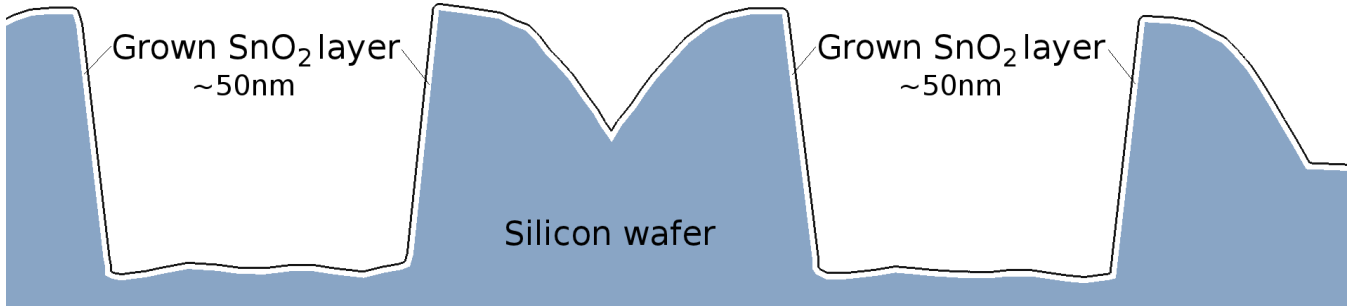
VII. CONCLUSION

In order to manufacture solid oxide fuel cells and smart gas sensor devices, the spray pyrolysis deposition technique is used to grow an ultrathin yttria-stabilized zirconia layer and a SnO₂ layer, respectively. Two different models are developed for the spray pyrolysis deposition technique, which depict two different experimental scenarios.

The first model, Model I, assumes that the accelerating forces are stronger than the retardant forces and that the droplet sizes are large enough to enable individual droplets to reach the wafer surface. Once they reach the surface, each droplet leaves a flat, disk-shaped imprint on the surface of the wafer. This is modeled by tracking the generation of droplets and their trajectory through the ambient as they are influenced by four external forces: gravity, electrical, Stokes, and thermophoretic.



(a) TEM image of a FIB cut with Pt on top, showing the geometry of a typical electrode structure with deposited SnO_2 layer.



(b) Simulated deposition of SnO_2 on a typical electrode geometry.

Fig 19. Image showing the (a) measured and (b) simulated deposited SnO_2 film as a results of spray pyrolysis deposition. The deposition is performed with the heated substrate at a temperature $T=400^\circ\text{C}$ for a time $t=30\text{s}$. The image is a side view of the FIB cut shown in Fig 2.

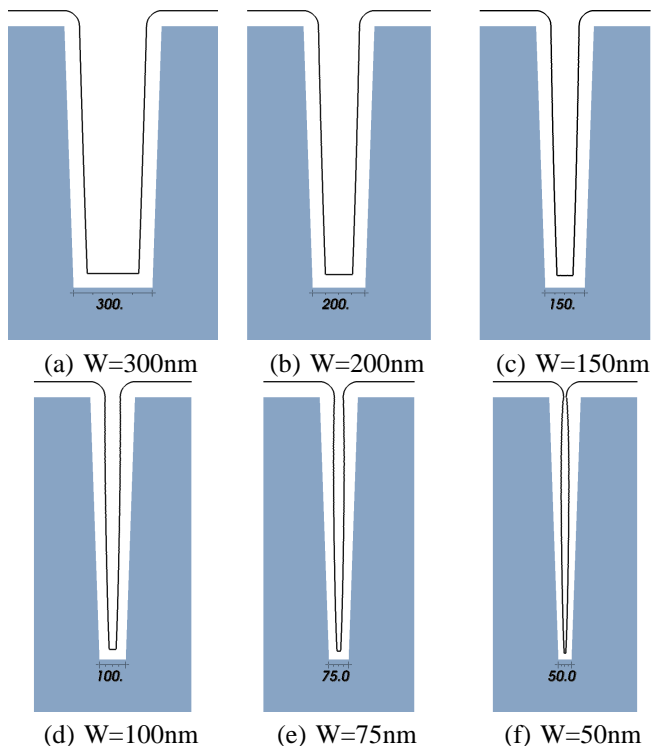


Fig 20. Sample spray pyrolysis deposition of SnO_2 simulation showing a 30s spray pyrolysis deposition at 400°C with a trench depth of 1000nm and widths ranging between (a) 300nm, (b) 200nm, (c) 150nm, (d) 100nm, (e) 75nm, and (f) 50nm. Sidewall angles are set to 2° and the resulting SnO_2 thickness is expected to be approximately 50nm.

The second model, Model II, deals with spray pyrolysis systems which produce very small droplets which reach the vicinity of the heated wafer surface and evaporate prior to deposition. Once they reach the surface, their deposition is

analogous to that of a CVD process and the model reflects this. A model which relates the deposited film thickness to the spray time and wafer temperature is derived. Within the simulator, the Monte Carlo method is used in combination with the Level Set framework in order to visualize the topography moving as a result of the deposition.

Both presented models have been implemented into a process simulator which can already handle many CMOS processes. This allows for an easy integration of these models within a sequence of CMOS processing steps.

APPENDIX

I - DERIVATION OF DROPLET TRANSPORT EQUATIONS: VELOCITY-DEPENDENT ACCELERATION

This section is devoted to describe the derivation of the equations of motion for a droplet experiencing a force in the direction of its motion, such as gravity as well as forces working against its motion like the thermophoretic force and the velocity-dependent Stokes force. For now it is assumed that there is no influence from the electric force on the droplet motion. The first step is to equate all forces acting on the droplet

$$F_{tot} = F_g + (F_{th}) + F_S, \quad (34)$$

where F_g is the force due to gravity, F_S is the Stokes force, and the thermophoretic force F_{th} is in brackets, because it is only included, when the droplet reaches the heat zone, and at that point, the radius must be modified according to its evaporation. However, for the following derivations, a constant radius has been assumed. Therefore, when the thermophoretic force is included, a smaller radius r_d is carried through the equations. The forces can be converted

to droplet acceleration using

$$a(t)_{tot} = a(t)_g + (a(t)_{th}) + a(t)_S, \quad (35)$$

where $a(t)_g$, $a(t)_{th}$, and $a(t)_S$ are the droplet accelerations due to gravity, the thermophoretic force, and the Stokes force, respectively. Since $F = m \cdot a$, then

$$a(t) = g + \left(\frac{F_{th}}{m} \right) + \frac{F_S}{m} \quad (36)$$

and the droplet mass m is given by

$$m = \frac{4\pi}{3} \rho_d r_d^3. \quad (37)$$

The explicit equation for the droplet acceleration can be derived by substituting the relevant forces and the droplet mass m into (36)

$$a(t) = \left[g + \left(-\frac{27 \eta_a^2 \kappa_a \nabla T}{4 \rho_a \rho_d T (2\kappa_a + \kappa_d) r^2} \right) \right] - \frac{9 \eta_a}{2 \rho_d r^2} v(t), \quad (38)$$

where the meaning and values for the droplet and ambient parameters in (38) can be found in the table from Appendix IV. In order to simplify the derivation, all constant values will be grouped together and only two constants will remain in the form of the independent constant a and constant b , which relates the velocity dependence of the acceleration

$$a = g + \left(-\frac{27 \eta_a^2 \kappa_a \nabla T}{4 \rho_a \rho_d T (2\kappa_a + \kappa_d) r^2} \right), \quad b = \frac{9 \eta_a}{2 \rho_d r^2} v(t), \quad (39)$$

allowing for (38) to be rewritten as

$$a(t) = a - b v(t), \quad (40)$$

The solution to (40) is found by first noting that it is a differential equation

$$\frac{dv(t)}{dt} = a - b v(t), \quad (41)$$

which can be re-written in the form

$$\frac{dv(t)}{dt} + b v(t) - a = 0 \quad (42)$$

and converted into Euler's characteristic equation

$$r + b = 0. \quad (43)$$

This characteristic equation only has one root, $r = -b$, meaning the velocity can be solved by writing

$$v(t) = A e^{-bt} + B, \quad (44)$$

where A and B are constants. In order to find A and B , two assumptions must be made: the initial velocity $v(0) = v_0$ is known and at some time t , the velocity will reach a terminal velocity due to the equivalent and opposite forces acting on the droplet, meaning $\frac{dv(t)}{dt}_{t=\infty} = 0$. Therefore, when t approaches infinity, $v(t)$ from (44) approaches B , meaning that B is the terminal velocity v_∞ . This can be substituted into (40) to obtain

$$0 = a - b B, \quad \text{then } B = \frac{a}{b}. \quad (45)$$

Now that B and $v(0)$ are known, they can be substituted into (44) to find A

$$v_0 = A + \frac{a}{b}, \quad \text{then } A = v_0 - \frac{a}{b}, \quad (46)$$

giving the final description for the velocity of the droplet at any time t

$$v(t) = v_0 e^{-bt} - \frac{a}{b} e^{-bt} + \frac{a}{b}. \quad (47)$$

In order to find the displacement of the droplet under the given forces, (47) can be integrated from $t = 0$, when the initial displacement d_0 is set to 0

$$d(t) = \int_0^t v(t) dt = \int_0^t \left(v_0 e^{-bt} - \frac{a}{b} e^{-bt} + \frac{a}{b} \right) dt. \quad (48)$$

resulting in

$$d(t) = \left[-\frac{v_0}{b} e^{-bt} + \frac{a}{b^2} e^{-bt} + \frac{a}{b} t \right]_0^t. \quad (49)$$

The displacement is then given by

$$d(t) = \frac{a}{b} t + \frac{a}{b^2} e^{-bt} - \frac{v_0}{b} e^{-bt} - \left(-\frac{v_0}{b} + \frac{a}{b^2} \right) \quad (50)$$

or

$$d(t) = \frac{1}{b} \left(v_0 - \frac{a}{b} \right) (1 - e^{-bt}) + \frac{a}{b} t. \quad (51)$$

The time t is needed in order to calculate the droplet displacement. As the droplet travels through the ambient, it is much easier to calculate the time required for the droplet to reach the wafer followed by the calculation of the radial direction displacement. This would make simulations much quicker than a discretization of the time t in order to follow the droplet trajectory. The time is found by inverting (51)

$$t = \frac{a W \left[\frac{(a - b v_0) \cdot e^{1 - \frac{b(v_0 + b d(t))}{a}}}{a} \right] - a + b v_0 + b^2 d(t)}{a b}, \quad (52)$$

where $W[\cdot]$ is the Lambert-W function which is solved iteratively and is defined by

$$z = W(z) e^{W(z)}. \quad (53)$$

APPENDIX

II - DERIVATION OF DROPLET TRANSPORT EQUATIONS: VELOCITY- AND DISPLACEMENT-DEPENDENT ACCELERATION

When the acceleration of a droplet also depends on the droplet's position in a simulation environment, or the displacement from its original position, such as is the case with the application of an electric force to a droplet's transport, the total force experienced by a droplet becomes

$$F_{tot} = F_g + (F_{th}) + F_S + F_e, \quad (54)$$

where F_e is the electric force and the acceleration becomes

$$a(t)_{tot} = a(t)_g + (a(t)_{th}) + a(t)_S + a(t)_e. \quad (55)$$

Acceleration due to the applied electric field is modeled as a linear displacement-dependent acceleration

$$c = \frac{6}{\rho_d} \sqrt{\frac{\gamma \epsilon_0}{r_d^3}} \cdot \frac{\Phi_0}{H} \cdot \frac{K_V}{\log(4H/R)} c_e, \quad (56)$$

while acceleration due to gravity and the Stokes component of the acceleration remain the same from the velocity-dependent acceleration derivation. Therefore, the following equation must be solved to find the droplet displacement after time t

$$a(t) = a - bv(t) + cd(t). \quad (57)$$

The equation can be re-written into a standard quadratic form, which is easier to solve

$$a(t) + bv(t) - cd(t) - a = 0. \quad (58)$$

Noting that $a(t) = \frac{d^2 d(t)}{dt^2}$, $v(t) = \frac{dd(t)}{dt}$, and $d(t)$ is the displacement.

$$\frac{dd^2(t)}{dt^2} + b \frac{dv(t)}{dt} - cd(t) - a = 0. \quad (59)$$

Using the Laplace method for solving differential equations, the characteristic equation, (59) can be re-written using s to depict a derivation step and r_i to depict the roots of equations. Assuming the initial velocity v_0 and initial displacement d_0 , (59) becomes

$$(s^2 d(t) - s d_0 - v_0) + b(s d(t) - d_0) - cd(t) - \frac{a}{s} = 0. \quad (60)$$

Multiplying by s gives

$$s^3 d(t) - s^2 d_0 - s v_0 + s^2 b d(t) - s b d_0 - s c d(t) - a = 0. \quad (61)$$

Isolating for $d(t)$ gives

$$d(t) = \frac{s^2 d_0 + s(v_0 + b d_0) + a}{s(s^2 + s b - c)}, \quad (62)$$

which is then split according to the numerator's power of s using partial fractional decomposition

$$d(t) = \underbrace{\frac{s d_0}{(s^2 + s b - c)}}_{\text{System 1}} + \underbrace{\frac{v_0 + b d_0}{(s^2 + s b - c)}}_{\text{System 2}} + \underbrace{\frac{a}{s(s^2 + s b - c)}}_{\text{System 3}}. \quad (63)$$

The roots of the equation can be found by finding s values for which (63) is invalid, or infinity. These roots are

$$r_1 = \frac{-b + \sqrt{b^2 + 4c}}{2}, \quad r_2 = \frac{-b - \sqrt{b^2 + 4c}}{2}, \quad r_3 = 0. \quad (64)$$

In order to find the final equation for the displacement $d(t)$, a solution to each system in (63) must be found and added together

• **System 1**

System 1 is set up such that the two roots are separated

$$\frac{s d_0}{(s^2 + s b - c)} = \frac{A_1}{(s - r_1)} + \frac{B_1}{(s - r_2)}, \quad (65)$$

where A_1 and B_1 are parameters to solve the displacement due to System 1

$$d(t)_1 = A_1 e^{(-r_1 t)} + B_1 e^{(-r_2 t)}. \quad (66)$$

A_1 and B_1 are found using (65)

$$A_1 = d_0 \left(1 - \frac{r_2}{r_2 - r_1} \right), \quad \text{and } B_1 = d_0 \frac{r_2}{r_2 - r_1}. \quad (67)$$

• **System 2**

Similar to System 1, System 2 is set up, separating the effects from the two roots

$$\frac{v_0 + b d_0}{(s^2 + s b - c)} = \frac{A_2}{(s - r_1)} + \frac{B_2}{(s - r_2)}, \quad (68)$$

where A_2 and B_2 are parameters to solve the displacement due to System 2

$$d(t)_2 = A_2 e^{(-r_1 t)} + B_2 e^{(-r_2 t)}. \quad (69)$$

A_2 and B_2 are found using (68)

$$A_2 = -\frac{v_0 + b d_0}{r_2 - r_1}, \quad \text{and } B_2 = \frac{v_0 + b d_0}{r_2 - r_1}. \quad (70)$$

• **System 3**

System 3 has an additional root involvement from the presence of s in the denominator, so the system is set up as

$$\frac{a}{s(s^2 + s b - c)} = \frac{A_3}{(s - r_1)} + \frac{B_3}{(s - r_2)} + \frac{C_3}{s}, \quad (71)$$

where A_3 , B_3 , and C_3 are parameters to solve the displacement due to System 3

$$d(t)_3 = A_3 e^{(-r_1 t)} + B_3 e^{(-r_2 t)} + C_3. \quad (72)$$

A_3 , B_3 , and C_3 are found using (71)

$$A_3 = \frac{a}{r_1(r_1 - r_2)}, \quad B_3 = \frac{a}{r_2(r_2 - r_1)}, \quad \text{and } C_3 = \frac{a}{r_1 r_2}. \quad (73)$$

After combining all three systems, the equation which governs the displacement at time t due to velocity and displacement-dependent acceleration is given by

$$d(t) = (A_1 + A_2 + A_3) e^{-r_1 t} + (B_1 + B_2 + B_3) e^{-r_2 t} + C_3. \quad (74)$$

It should be noted that, if the initial displacement is set to 0, then $A_1 = B_1 = 0$. Similarly, if the initial velocity is also set to 0, then $A_2 = B_2 = 0$, significantly reducing the complexity of the problem.

APPENDIX

III - DROPLET RADIUS DISTRIBUTION

The random distribution for the droplet radius for spray pyrolysis deposition Model I (17) is derived in this section. The volume fraction is evenly distributed along the droplets whose radii range from $r_{min} = 2.5 \mu m$ to $r_{max} = 55 \mu m$. Therefore, the first step is to relate the radius distribution linearly to a value $x \in [0, 1]$ so that as x goes from 0 to 1, r_d goes from r_{min} to r_{max} :

$$r_d(x) = (r_{max} - r_{min})x + r_{min}, \quad \text{where } x \in [0, 1]. \quad (75)$$

Next, the assertion is made that x represents the evenly distributed volume number fraction, or normalized volume

$\xi = x$. Using the equation for the volume of a sphere, the relationship between volume and radius is established as

$$V_{sphere} = \frac{4\pi}{3} r_d^3. \quad (76)$$

Therefore, when the volume is evenly distributed, the effect on the radius will be $\xi_V \propto \frac{1}{r_d^3}$.

We know that the radius distribution should follow the equation

$$r_\xi = \frac{C}{r_d^3}, \quad (77)$$

where C is a normalization constant which must be found, r_ξ is the randomly distributed radius, and r_d is the radius relating r_{min} and r_{max} to an even volume distribution $\xi_V \in [0, 1]$ from (75)

$$r_\xi = \frac{C}{[(r_{max} - r_{min}) \xi_V + r_{min}]^3}. \quad (78)$$

Inverting (78) to solve for ξ_V allows to find the cumulative probability density (CPD) function $\Phi(r_\xi)$

$$\Phi(r_\xi) = \xi_V = \frac{1}{r_{max} - r_{min}} \left[\left(\frac{C}{r_\xi} \right)^{1/3} - r_{min} \right]. \quad (79)$$

The derivative of (79) gives the probability density function (PDF)

$$f(r_\xi) = \frac{d\Phi(r_\xi)}{dr_\xi} = -\frac{C^{1/3}}{3} \cdot \frac{1}{r_{max} - r_{min}} \cdot r_\xi^{-4/3}, \quad (80)$$

where it can be noted that the last r_{min} term from (79) has disappeared. The only non-constant term in (80) is $r_\xi^{-4/3}$, therefore a replacement constant, which will be the new normalization constant is introduced for simplicity

$$A \equiv -\frac{C^{1/3}}{3} \cdot \frac{1}{r_{max} - r_{min}} \quad (81)$$

and (80) can be rewritten to

$$f(r_\xi) = A \cdot r_\xi^{-4/3}. \quad (82)$$

Using the PDF from (82), we can now proceed to find the normalized distribution r_ξ , but first the normalization constant A must be found by integrating (82) with respect to r_ξ from r_{min} to r_{max} and equating the integral to 1

$$\int_{r_{min}}^{r_{max}} f(r_\xi) dr_\xi = \int_{r_{min}}^{r_{max}} A \cdot r_\xi^{-4/3} dr_\xi = 1, \quad (83)$$

which can be solved to

$$-3A \left[\left(\frac{1}{r_{max}} \right)^{1/3} - \left(\frac{1}{r_{min}} \right)^{1/3} \right] = 1, \quad (84)$$

giving the normalization constant A

$$A = -\frac{1}{3 \left[r_{max}^{-1/3} - r_{min}^{-1/3} \right]} \quad (85)$$

and the normalized PDF

$$f(r_d) = -\frac{1}{3 \left[r_{max}^{-1/3} - r_{min}^{-1/3} \right]} \cdot r_d^{-4/3}. \quad (86)$$

Now one can integrate the normalized PDF from r_{min} to r_ξ to find the CPD

$$\int_{r_{min}}^{r_\xi} f(r) dr = \frac{r_\xi^{-1/3} - r_{min}^{-1/3}}{r_{max}^{-1/3} - r_{min}^{-1/3}} = \xi_V \quad (87)$$

and invert the CPD to find the quantile function and solve for r_ξ

$$r_\xi = \left\{ \xi_V \cdot \left[(r_{max})^{-1/3} - (r_{min})^{-1/3} \right] + (r_{min})^{-1/3} \right\}^{-3}, \quad (88)$$

which gives the equation for the radius distribution r_ξ between r_{min} and r_{max} when the volume number fraction ξ_V is evenly distributed and $\xi_V \in [0, 1]$.

ACKNOWLEDGMENT

The authors would like to thank Martina Dienstleder with the Institute for Electron Microscopy and Fine Structure Research, Graz University of Technology for the FIB preparation.

REFERENCES

- [1] G. L. Messing, S.-C. Zhang, and G. V. Jayanthi, "Ceramic powder synthesis by spray pyrolysis," *Journal of the American Ceramic Society*, vol. 76, no. 11, pp. 2707–2726, 1993.
- [2] L. Filipovic, S. Selberherr, G. C. Mutinati, E. Brunet, S. Steinhauer, A. Köck, J. Teva, J. Kraft, J. Siegert, and F. Schrank, "Modeling spray pyrolysis deposition," in *Proceedings of the World Congress on Engineering*, vol. 2, 2013, pp. 987–992.
- [3] D. Perednis, "Thin film deposition by spray pyrolysis and the application in solid oxide fuel cells," Dissertation, Eidgenössische Technische Hochschule (ETH) Zürich, 2003, <http://e-collection.library.ethz.ch/eserv/eth:26881/eth-26881-02.pdf>.
- [4] A. de Frank Bruijn and G. J. Janssen, "Pem fuel cell materials: Costs, performance and durability," in *Fuel Cells*. Springer, 2013, pp. 249–303.
- [5] "Comparison of fuel cell technologies," U.S. Department of Energy: Energy Efficiency & Renewable Energy (EERE) Fuel Cells Technologies Program, February 2011, http://www1.eere.energy.gov/hydrogenandfuelcells/fuelcells/pdfs/fc_comparison_chart.pdf.
- [6] B. Qiu, B. Lin, L. Qiu, and F. Yan, "Alkaline imidazolium-and quaternary ammonium-functionalized anion exchange membranes for alkaline fuel cell applications," *Journal of Materials Chemistry*, vol. 22, no. 3, pp. 1040–1045, 2012.
- [7] K. Kargupta, S. Saha, D. Banerjee, M. Seal, and S. Ganguly, "Performance enhancement of phosphoric acid fuel cell by using phosphosilicate gel based electrolyte," *Journal of Fuel Chemistry and Technology*, vol. 40, no. 6, pp. 707–713, 2012.
- [8] T. Watanabe, "Molten carbonate fuel cells," in *Handbook of Climate Change Mitigation*. Springer, 2012, pp. 1729–1754.
- [9] C. Zuo, M. Liu, and M. Liu, "Solid oxide fuel cells," in *Sol-Gel Processing for Conventional and Alternative Energy*. Springer, 2012, pp. 7–36.
- [10] M. Ortel, Y. S. Trostyanskaya, and V. Wagner, "Spray pyrolysis of ZnO-TFTs utilizing a perfume atomizer," *Solid-State Electronics*, vol. 86, no. 0, pp. 22 – 26, 2013.
- [11] S. Shinde, G. Patil, D. Kajale, V. Gaikwad, and G. Jain, "Synthesis of ZnO nanorods by spray pyrolysis for H₂S gas sensor," *Journal of Alloys and Compounds*, vol. 528, no. 0, pp. 109 – 114, 2012.
- [12] A. Bouaoud, A. Rmili, F. Ouachtari, A. Louardi, T. Chtouki, B. Elidrissi, and H. Erguig, "Transparent conducting properties of Ni doped zinc oxide thin films prepared by a facile spray pyrolysis technique using perfume atomizer," *Materials Chemistry and Physics*, vol. 137, no. 3, pp. 843 – 847, 2013.
- [13] M. Prasad, V. Sahula, and V. Khanna, "Design and fabrication of Si-diaphragm, ZnO piezoelectric film-based MEMS acoustic sensor using SOI wafers," *IEEE Transactions on Semiconductor Manufacturing*, vol. 26, no. 2, pp. 233–241, 2013.
- [14] G. Patil, D. Kajale, V. Gaikwad, and G. Jain, "Spray pyrolysis deposition of nanostructured tin oxide thin films," *ISRN Nanotechnology*, vol. 2012, 2012.

APPENDIX

IV - CHARACTERISTICS OF THE PRECURSOR SOLUTIONS USED FOR THE SIMULATIONS

Droplet properties

| | Ethanol | Water |
|---|--------------------------------------|--------------------------------------|
| Droplet conductivity (κ_d) | 0.19 W/m · K | 0.609W/m · K |
| Droplet density (ρ_d) | 789 kg/m ³ | 998kg/m ³ |
| Absolute viscosity (η_d) | 0.00116 N · s/m ² | 0.01 N · s/m ² |
| Surface tension (γ) | 0.022 N/m | 0.072 N/m |
| Permittivity (ϵ) | 25 ϵ_0 | 80.1 ϵ_0 |
| Molar weight (M_W) | 46.1 g/mole | 18.0 g/mole |
| Average diffusion coefficient ($D_{v,f}$) | $6.314 \times 10^{-22} \times T/r$ | $7.325 \times 10^{-23} \times T/r$ |
| Saturation vapor pressure (SVP) | 5380 Pa | 2340 Pa |
| Boiling point (1atm) | 351.5 K | 373 K |
| Maximum droplet charge (q_{max}) | $1.11 \times 10^{-5} \times r^{3/2}$ | $2.01 \times 10^{-5} \times r^{3/2}$ |

Air/ambient properties

| | |
|---|------------------------------------|
| Air viscosity (η_a) | $2.2 \times 10^{-5} N \cdot s/m^2$ |
| Air density (ρ_a) | 1.29 kg/m ³ |
| Air thermal conductivity (κ_a) | 0.025 W/m · K |
| Gas constant (R) | 8.3144621 m · N/K · mol |

Simulation properties

| | ESD | PSD |
|---|----------------------------------|---------------------------------|
| Minimum droplet radius (r_{min}) | 2.5 μm | 1.5 μm |
| Maximum droplet radius (r_{max}) | 55 μm | 5 μm |
| Atomizer height (H) | 270mm | $H_x=200mm, H_y=100mm$ |
| Droplet distribution angle (θ_d) | 45° | 12° |
| Flow rate | 2.8ml/h | < 3.1ml/h |
| Electric potential (Φ_0) | 10kV | - |
| K_V | ~ 1 | - |
| Evaporation parameter (q_0) | $\sim 373 \mu m^2/s \cdot K$ | $\sim 88 \mu m^2/s \cdot K$ |
| Evaporation parameter (q_1) | $\sim 8.91 \times 10^{-5}/\mu m$ | $\sim 4.3 \times 10^{-3}/\mu m$ |
| Temperature (T) | 523K | 673K |
| Temperature gradient (∇T) | 100,000K/m | 30,000K/m |

- [15] G. Mutinati, E. Brunet, S. Steinhauer, A. Köck, J. Teva, J. Kraft, J. Siegert, F. Schrank, and E. Bertagnoli, "CMOS-integrable ultrathin SnO₂ layer for Smart Gas sensor devices," *Procedia Engineering*, vol. 47, pp. 490–493, 2012.
- [16] E. Brunet, T. Maier, G. Mutinati, S. Steinhauer, A. Köck, C. Gspan, and W. Grogger, "Comparison of the gas sensing performance of SnO₂ thin film and SnO₂ nanowire sensors," *Sensors and Actuators B: Chemical*, vol. 165, no. 1, pp. 110–118, 2012.
- [17] I. Volintiru, A. de Graaf, J. Van Deelen, and P. Poodt, "The influence of methanol addition during the film growth of SnO₂ by atmospheric pressure chemical vapor deposition," *Thin Solid Films*, vol. 519, no. 19, pp. 6258–6263, 2011.
- [18] J. Boltz, D. Koehl, and M. Wuttig, "Low temperature sputter deposition of SnO_x: Sb films for transparent conducting oxide applications," *Surface and Coatings Technology*, vol. 205, no. 7, pp. 2455–2460, 2010.
- [19] S. Sinha, R. Bhattacharya, S. Ray, and I. Manna, "Influence of deposition temperature on structure and morphology of nanostructured SnO₂ films synthesized by pulsed laser deposition," *Materials letters*, vol. 65, no. 2, pp. 146–149, 2011.
- [20] D. M. Carvalho, J. L. Maciel Jr, L. P. Ravaro, R. E. Garcia, V. G. Ferreira, and L. V. Scalvi, "Numerical simulation of the liquid phase in SnO₂ thin film deposition by sol-gel-dip-coating," *Journal of sol-gel science and technology*, vol. 55, no. 3, pp. 385–393, 2010.
- [21] W. Göpel and K. Schierbaum, "SnO₂ sensors: current status and future prospects," *Sensors and Actuators B: Chemical*, vol. 26-27, pp. 1–12, 1995.
- [22] A. Tischner, T. Maier, C. Stepper, and A. Köck, "Ultrathin SnO₂ gas sensors fabricated by spray pyrolysis for the detection of humidity and carbon monoxide," *Sensors and Actuators B: Chemical*, vol. 134, no. 2, pp. 796–802, 2008.
- [23] O. Ertl, "Numerical methods for topography simulation," Dissertation, Technischen Universität Wien, Fakultät für Elektrotechnik und Informationstechnik, May 2010, <http://www.iue.tuwien.ac.at/phd/ertl/>.
- [24] W. H. Press, *Numerical Recipes: The Art of Scientific Computing*, 3rd ed. Cambridge University Press, 2007.
- [25] B. Engquist and S. Osher, "Stable and entropy satisfying approximations for transonic flow calculations," *Mathematics of Computation*, vol. 34, no. 149, pp. 45–75, 1980.
- [26] J. A. Sethian, *Level Set Methods and Fast Marching Methods*, 2nd ed. Cambridge University Press, 1999.
- [27] A. Nakaruk and C. Sorrell, "Conceptual model for spray pyrolysis mechanism: fabrication and annealing of titania thin films," *Journal of Coatings Technology and Research*, vol. 7, no. 5, pp. 665–676, 2010.
- [28] R. R. Chamberlin and J. S. Skarman, "Chemical spray deposition process for inorganic films," *Journal of the Electrochemical Society*, vol. 113, no. 1, pp. 86–89, 1966.
- [29] G. Korotcenkov, V. Brinzari, J. Schwank, M. DiBattista, and A. Vasiliev, "Peculiarities of SnO₂ thin film deposition by spray pyrolysis for gas sensor application," *Sensors and Actuators B: Chemical*, vol. 77, no. 1–2, pp. 244–252, 2001.
- [30] S. Rozati and T. Ganj, "Transparent conductive Sn-doped indium oxide thin films deposited by spray pyrolysis technique," *Renewable Energy*, vol. 29, no. 10, pp. 1671–1676, 2004.
- [31] J. Manificier, J. Fillard, and J. Bind, "Deposition of In₂O₃-SnO₂ layers on glass substrates using a spraying method," *Thin Solid Films*, vol. 77, no. 1-3, pp. 67–80, 1981.
- [32] H. Koo, S. Hong, S. Ju, I. Seo, and Y. Kang, "PbO-B₂O₃-SiO₂ glass powders with spherical shape prepared by spray pyrolysis," *Journal of Non-Crystalline Solids*, vol. 352, no. 30–31, pp. 3270–3274, 2006.
- [33] F. Paraguay D., W. Estrada L., D. Acosta N., E. Andrade, and M. Miki-Yoshida, "Growth, structure and optical characterization of high quality ZnO thin films obtained by spray pyrolysis," *Thin Solid Films*, vol. 350, no. 1–2, pp. 192–202, 1999.
- [34] D. Perednis and L. J. Gauckler, "Solid oxide fuel cells with electrolytes prepared via spray pyrolysis," *Solid State Ionics*, vol. 166, no. 3-4, pp. 229–239, 2004.

- [35] J. B. Mooney and S. B. Radding, "Spray Pyrolysis Processing," *Annual Review of Materials Science*, vol. 12, no. 1, pp. 81–101, Aug. 1982.
- [36] S. Major, A. Banerjee, and K. Chopra, "Highly transparent and conducting indium-doped zinc oxide films by spray pyrolysis," *Thin Solid Films*, vol. 108, no. 3, pp. 333–340, 1983.
- [37] S. H. Ng, J. Wang, D. Wexler, S. Y. Chew, and H. K. Liu, "Amorphous carbon-coated silicon nanocomposites: a low-temperature synthesis via spray pyrolysis and their application as high-capacity anodes for lithium-ion batteries," *The Journal of Physical Chemistry C*, vol. 111, no. 29, pp. 11 131–11 138, 2007.
- [38] G. Blandenet, M. Court, and Y. Lagarde, "Thin layers deposited by the pyrosol process," *Thin Solid Films*, vol. 77, no. 1–3, pp. 81–90, 1981.
- [39] D. Perednis and L. J. Gauckler, "Thin film deposition using spray pyrolysis," *Journal of Electroceramics*, vol. 14, no. 2, pp. 103–111, 2005.
- [40] A. J. Kelly, "Charge injection electrostatic atomizer modeling," *Aerosol Science and Technology*, vol. 12, no. 3, pp. 526–537, 1990.
- [41] A. Lefebvre, *Atomization and sprays*. Hemisphere Publishing Corporation, 1989.
- [42] A. Revuelta, J. Rodríguez-Rodríguez, and C. Martínez-Bazán, "On the breakup of bubbles at high reynolds numbers and subcritical weber numbers," *European Journal of Mechanics-B/Fluids*, vol. 27, no. 5, pp. 591–608, 2008.
- [43] "Spraying Systems Co., Volume median diameter versus air pressure at constant liquid pressures," data Sheet No. 36892-8M.
- [44] J. C. Vigié and J. Spitz, "Chemical vapor deposition at low temperatures," *Journal of The Electrochemical Society*, vol. 122, no. 4, pp. 585–588, 1975.
- [45] W. Siefert, "Properties of thin In_2O_3 and SnO_2 films prepared by corona spray pyrolysis, and a discussion of the spray pyrolysis process," *Thin Solid Films*, vol. 120, no. 4, pp. 275–282, 1984.
- [46] I. W. Lenggoro, "An experimental and modeling investigation of particle production by spray pyrolysis using a laminar flow aerosol reactor," *Journal of Materials Research*, vol. 15, no. 3, pp. 733–743, 2000.
- [47] L. Filipovic, "Topography simulation of novel processing techniques," Dissertation, Technischen Universität Wien, Fakultät für Elektrotechnik und Informationstechnik, December 2012, <http://www.iue.tuwien.ac.at/phd/filipovic/>.
- [48] O. Wilhelm, "Electrohydrodynamic spraying – transport, mass and heat transfer of charged droplets and their application to the deposition of thin functional films." Dissertation, Swiss Federal Institute of Technology Zurich - Eidgenössische Technische Hochschule (ETH) Zürich, 2004, <http://fex-dev2.ethz.ch/eserv/eth:27191/eth-27191-02.pdf>.
- [49] A. Gañán-Calvo, J. Lasheras, J. Dávila, and A. Barrero, "The electrostatic spray emitted from an electrified conical meniscus," *Journal of Aerosol Science*, vol. 25, no. 6, pp. 1121–1142, 1994.
- [50] D. Veberic, "Having Fun with Lambert $W(x)$ Function," *ArXiv e-prints*, Mar. 2010, <http://adsabs.harvard.edu/abs/2010arXiv1003.1628V>.
- [51] J. Greenwood, "The correct and incorrect generation of a cosine distribution of scattered particles for Monte-Carlo modelling of vacuum systems," *Vacuum*, vol. 67, no. 2, pp. 217–222, 2002.